nature climate change

ARTICLES

PUBLISHED ONLINE: 4 SEPTEMBER 2017 | DOI: 10.1038/NCLIMATE3381

Change in the magnitude and mechanisms of global temperature variability with warming

Patrick T. Brown[1]*, Yi Ming[2], Wenhong Li[3] and Spencer A. Hill[4,5]

Natural unforced variability in global mean surface air temperature (GMST) can mask or exaggerate human-caused global warming, and thus a complete understanding of this variability is highly desirable. Significant progress has been made in elucidating the magnitude and physical origins of present-day unforced GMST variability, but it has remained unclear how such variability may change as the climate warms. Here we present modelling evidence that indicates that the magnitude of low-frequency GMST variability is likely to decline in a warmer climate and that its generating mechanisms may be fundamentally altered. In particular, a warmer climate results in lower albedo at high latitudes, which yields a weaker albedo feedback on unforced GMST variability. These results imply that unforced GMST variability is dependent on the background climatological conditions, and thus climate model control simulations run under perpetual pre-industrial conditions may have only limited relevance for understanding the unforced GMST variability of the future.

Global mean surface air temperature (GMST) is one of the most well-recognized metrics of climate change both contemporarily and through deep time. On centennial timescales, positive external radiative forcings, mostly due to increased concentrations of well-mixed greenhouse gases, are currently causing pronounced GMST warming[1]. However, unforced GMST change, which is spontaneously generated from interactions internal to the ocean–atmosphere–land system, superimposes variability on this long-term warming that can alternatively mask or exaggerate externally forced signals for years to decades at a time[2–4]. Thus, to attribute past changes to human activities or to accurately predict climate change on policy-relevant decadal timescales, robust understanding of both the magnitude and mechanisms responsible for unforced GMST variability is critical.

Three principal methodologies are typically used to surmise information on the physics and statistics of contemporary unforced GMST variability: unforced GMST variability is studied using the output of coupled atmosphere–ocean global climate models run under perpetual pre-industrial boundary conditions[5–10]; unforced GMST variability is studied using observed or reconstructed data sets spanning the most recent century to approximately the past millennium[11–17]; and/or unforced GMST variability is studied in climate model experiments that incorporate historical estimates of time-varying external radiative forcings[2,9,18–21]. Such studies could be used to draw inferences about unforced GMST variability in the future if it is assumed that GMST variability is more-or-less independent of the climatological GMST. However, given that many features of the climate system are not independent of absolute temperature, it is plausible that the physics and statistics of GMST variability might not be conserved across a wide range of climatological GMST values. For example, a warmer climate is likely to be characterized by changes in mean sea-ice extent[22], hydrology[22], upper-ocean stratification[23], and surface energy budget partitioning[24], all of which could impact GMST variability.

Previous work has emphasized changes in local surface air temperature (SAT) variability with warming[25–32], but the purpose of the present study is to examine how GMST variability may or may not change as the underlying climate warms. We perform detailed analysis on an experiment utilizing the fully coupled Geophysical Fluid Dynamics Laboratory (GFDL) CM3 climate model, and we supplement this with results from an atmosphere-only GFDL AM3 experiment as well as relevant results from Phase 5 of the Coupled Model Intercomparison Project (CMIP5; ref. 33) archive (see Methods).

Response of GMST variability to GMST warming

First we compare approximately nine centuries of variability in the fully coupled GFDL CM3 model run under perpetual pre-industrial radiative boundary conditions with variability in the same model after the climate system has equilibrated to a doubling of atmospheric CO_2 concentration (Fig. 1). The warming of the climatological GMST (+4.8 K) is associated with a ∼43% reduction (∼9% reduction per kelvin of GMST warming) in the temporal standard deviation of low-frequency GMST variability (identified with a 15-year lowess[34] filter; see blue and red lines in Fig. 1a,b). The reduction in variability is not specific to the definition of low-frequency timescale—it occurs on virtually all timescales longer than approximately a decade (see blue and red lines in Fig. 1c).

Not only is there a large change in the magnitude of low-frequency GMST variability between the GFDL CM3 pre-industrial control and $2 \times CO_2$ runs, there is also an alteration in the geographic origin of GMST variability. Figure 1d,e shows the local SAT regression against low-frequency GMST variability, which highlights the regions that contribute the most to GMST variability in each run. Stippling represents 'regions of significant influence'[5] on GMST variability, which are locations that have a statistically significant relationship between local SAT and GMST variability, have local SAT variability that tends to lead GMST variability

[1]Department of Global Ecology, Carnegie Institution for Science, Stanford, California 94305, USA. [2]Geophysical Fluid Dynamics Laboratory/NOAA, Princeton, New Jersey 08540, USA. [3]Earth and Ocean Sciences, Nicholas School of the Environment, Duke University, Durham, North Carolina 27708, USA. [4]Department of Atmospheric and Oceanic Sciences, University of California, Los Angeles, California 90095, USA. [5]Division of Geological and Planetary Sciences, California Institute of Technology, Pasadena, California 91125, USA. *e-mail: pbrown@carnegiescience.edu

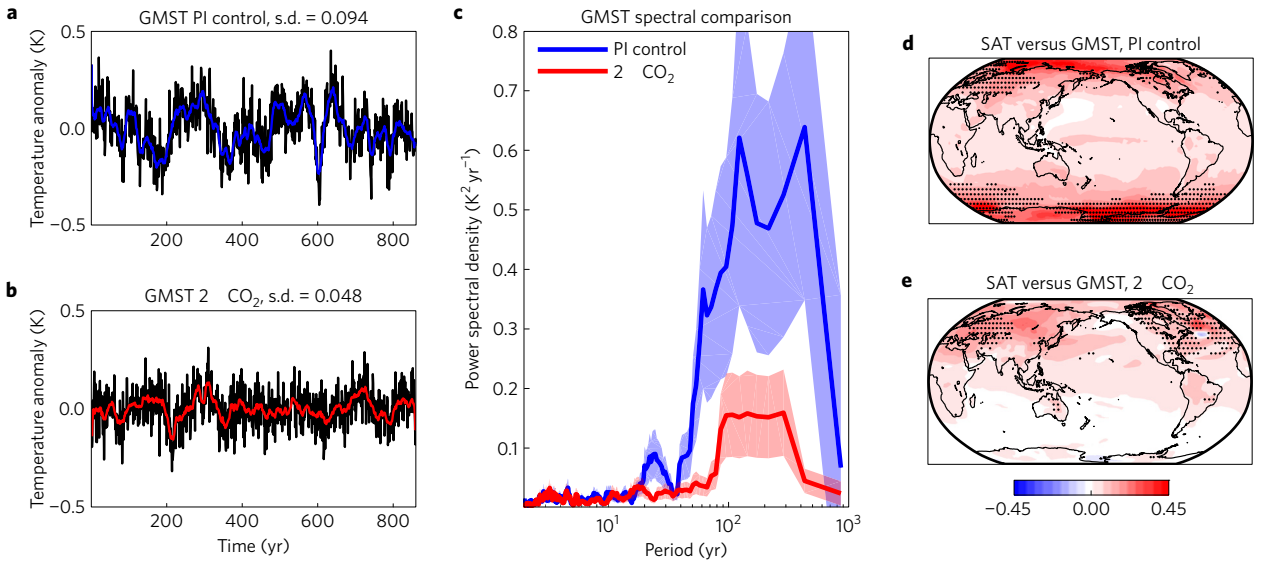

Figure 1 | Magnitude and geographic origin of GMST variability in the GFDL CM3 pre-industrial control and 2 × CO_2 runs. a, Annual mean time series of GMST variability (black) in the pre-industrial (PI) control run with the low-frequency component (15-year lowess smooth) shown in blue. **b**, As in **a** but in the 2 × CO_2 run. The time series in **a** and **b** are displayed as anomalies relative to their own GMST climatology but this climatology is 4.8 K warmer in the 2 × CO_2 run. **c**, Power spectral density (smoothed with a 9-period running mean) of the two time series shown in **a** (blue) and **b** (red) with 1σ confidence intervals displayed. **d**, Local low-frequency SAT variability regressed against the standard deviation of low-frequency GMST variability in the pre-industrial control run. **e**, As in **d** but for the 2 × CO_2 run. Stippling in **d** and **e** represents 'regions of significant influence'[5], which highlight the locations (and by proxy modes of variability) that have the most influence on GMST variability (see main text, and ref. 5 for more details).

in time, and have local SAT variability that tends to enhance the magnitude of GMST variability. In the pre-industrial control run, low-frequency GMST variability (hereafter, GMST variability) is primarily associated with SAT variability over the Southern Ocean and Antarctica (Fig. 1d). In the 2 × CO_2 run, however, the origin of GMST variability shifts to be almost exclusively Northern Hemispheric in origin (Fig. 1e). In particular, GMST variability becomes much more associated with the model's Atlantic Multidecadal Oscillation (AMO) in the 2 × CO_2 run ($r^2 = 0.62$) compared with the pre-industrial control run ($r^2 = 0.36$), even though the magnitude of AMO variability does not change between the two runs (Supplementary Fig. 1).

Mechanisms underlying the change in GMST variability

Unforced variability in GMST can result from an internally generated change in the net exchange of heat between the ocean and atmosphere[35–38] and/or from an internally generated change in Earth's top-of-atmosphere (TOA) energy budget[6,39,40]. Therefore, insight into the physical explanations for unforced GMST variability can be gained by investigating lagged regression coefficients (cross-regressions) between GMST and the net anomalous downward TOA energy flux ($\downarrow N$) as well the net anomalous upward surface energy flux ($\uparrow Q$) (Fig. 2).

In the pre-industrial control run, positive $\downarrow N$ anomalies tend to precede positive GMST anomalies in time (black solid line in Fig. 2a) and negative $\uparrow Q$ anomalies tend to precede positive GMST anomalies in time (black solid line in Fig. 2c), indicating a tendency for net flow of energy from space to the ocean concurrent with unforced GMST warming events. This relationship suggests that internally generated $\downarrow N$ imbalances tend to enhance GMST variability. Of the four linearly additive components of $\downarrow N$ (clear-sky short-wave ($\downarrow$clear SW); clear-sky long-wave ($\downarrow$clear LW); cloud radiative effect short-wave ($\downarrow$cloud SW); cloud radiative effect long-wave ($\downarrow$cloud LW); see Methods), only the $\downarrow$clear LW damps GMST variability (red solid line in Fig. 2a). Both the $\downarrow$cloud LW and $\downarrow$cloud SW components enhance GMST variability, but the largest amplifying contribution comes from the $\downarrow$clear SW component (blue dashed line Fig. 2a). The short-wave components of the energy budget, both at the TOA and the surface (blue dashed line in Fig. 2c), tend to lead GMST variability in time and thus appear to partially drive GMST perturbations in the pre-industrial control run.

The spatial distribution of anomalous energy fluxes indicates that the Southern Ocean is a key region responsible for producing the $\downarrow N$ variability that enhances GMST variability in the pre-industrial control run. The dynamics of this Southern Ocean variability appear to be consistent with those expounded on in previous studies[41–43]. Specifically, it has been shown that southward-flowing North Atlantic Deep Water can deposit relatively warm, salty water at intermediate depths in the Southern Ocean. A large reservoir of heat can build up if convection is initially inhibited due to a relatively fresh surface layer and/or the presence of surface sea ice that obstructs air–sea heat exchange. Eventually, stochastic forcing via wind stress or surface salinity anomalies can cause the onset of convection (represented by deepening of the mixed layer; Supplementary Fig. 4e). During convection, saltier water from mid-depth is transported to the surface where a rise in salinity occurs (Supplementary Fig. 4f). As convection continues, substantial anomalous surface heat flux from the high-latitude Southern Ocean to the atmosphere occurs (Supplementary Fig. 5b) realized primarily in the sensible and latent heat flux components (Supplementary Fig. 5c,d). The excess energy is not damped to space locally, as a large reduction in sea-ice extent causes a positive anomalous $\downarrow$clear SW flux (Supplementary Fig. 6c), especially in the summer (Supplementary Fig. 6i), and a net positive $\downarrow N$ over the Southern Ocean (Supplementary Fig. 6b).

In the 2 × CO_2 run, the relationship between GMST, $\downarrow N$ and $\uparrow Q$ is fundamentally altered. Specifically, in the 2 × CO_2 run, anomalous GMST warmth tends to be preceded for several years by negative $\downarrow N$ values, in direct contrast to the pre-industrial control run. This alteration of the relationship between GMST and anomalous energy flow can be traced primarily to changes in the summer half-year (Supplementary Figs 2 and 3). In particular, the 2 × CO_2 run experiences a large reduction in the $\downarrow$clear SW component's contribution to GMST change (see blue dashed line in

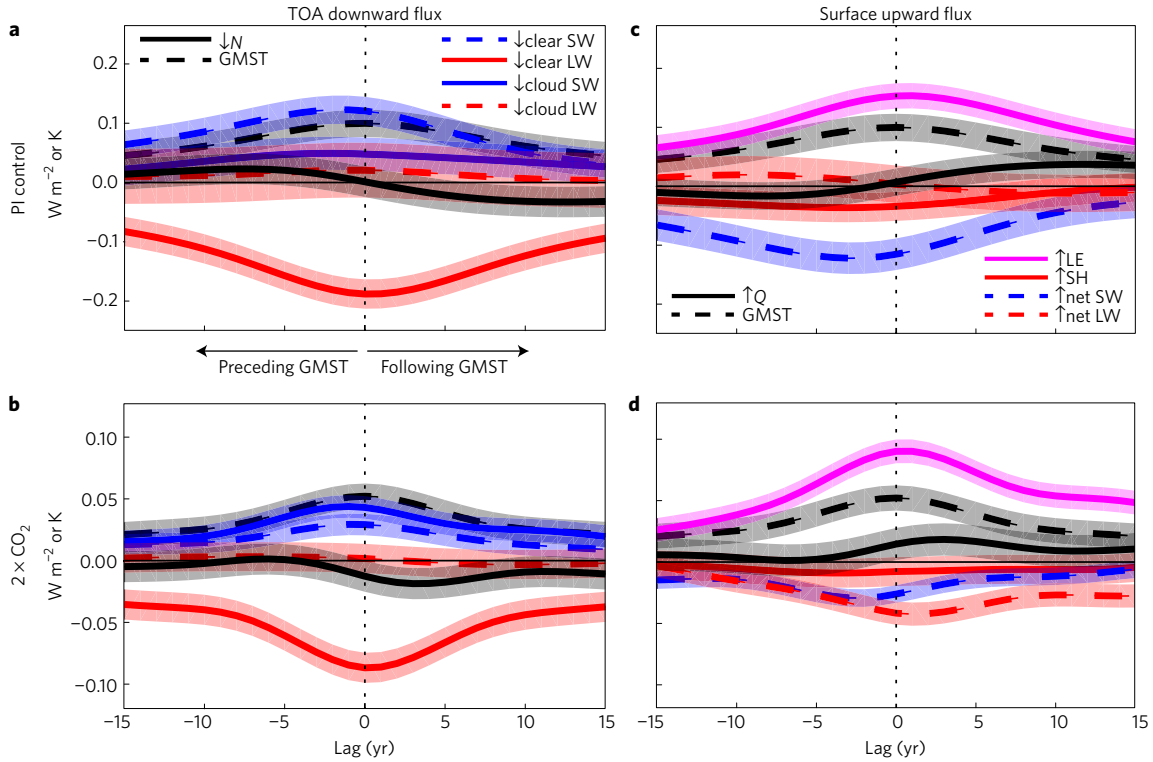

Figure 2 | Relationship between GMST and the TOA and surface energy budgets in the GFDL CM3 pre-industrial control and 2 × CO_2 runs. **a**–**d**, Cross-regression (lagged linear least-squares regression coefficients) between the low-frequency component of the labelled variables and the standard deviation of the low-frequency component of GMST. TOA components are shown in **a**,**b** and surface components are shown in **c**,**d** for the pre-industrial control run (**a**,**c**) and the 2 × CO_2 run (**b**,**d**). Note that the *y* axis spans a smaller range in the 2 × CO_2 run (**b**,**d**), indicating that the magnitude of variability tends to be smaller. TOA components (**a**,**b**) are positive down while surface components (**c**,**d**) are positive up. The dashed black line is GMST regressed against normalized GMST. The thickness of the confidence intervals represents the 2σ range of regression coefficients between time series with similar autocorrelation but with no relation to one and other. See Methods section for further details on the calculation of the confidence intervals.

Fig. 2a,b, noting that the *y* axis spans a smaller range in Fig. 2b than in Fig. 2a), which is primarily due to a reduction in its summertime magnitude (see blue dashed line in Supplementary Fig. 2c,d). This effect is also apparent in the net surface short-wave component (see blue dashed line in Fig. 2c,d and Supplementary Fig. 3c,d).

The 2 × CO_2 run exhibits GMST variability that is associated with the model's AMO (Fig. 1e). This is consistent with an enhanced contribution of North Atlantic latent and sensible heat flux to GMST variability in this run (Supplementary Fig. 9c,d). Additionally, since short-wave cloud feedback enhances the AMO[44], the 2 × CO_2 run is also characterized by a positive change in the contribution of ↓N to GMST variability over the North Atlantic (Fig. 3e,b). Despite this local increase, there is an overall reduction in the ↓N contribution to GMST variability between the pre-industrial and 2 × CO_2 runs primarily due to a reduction over the Southern Ocean (Fig. 3b). Specifically, over the Southern Ocean, climatological GMST warming is associated with a reduction in the climatological sea-ice extent and associated climatological albedo (Supplementary Fig. 7c). This causes a reduced contribution of ↓clear SW (Fig. 3c) and thus ↓N to GMST variability. Seasonally, the summer half-year produces most of the radiative change (see Supplementary Fig. 7i,o) because of the vast seasonal difference in incident solar radiation at high latitudes.

Additionally, GMST warming has been shown to be associated with stratification of the Southern Ocean and a reduced propensity for the kind of sustained open-ocean convection that appeared to influence GMST variability in the pre-industrial control run[23]. Indeed, the 2 × CO_2 run shows a reduction in Southern Ocean convection (Supplementary Fig. 10e), latent heat flux (Supplementary Fig. 9c), and sensible heat flux (Supplementary Fig. 9d) associated with GMST variability.

The changes in the magnitude and mechanisms of GMST variability apparent in the GFDL CM3 model are qualitatively reproduced in aggregate results from a subset of other CMIP5 models (see Methods and Supplementary Table 1). Specifically, we find that CMIP5 models show a statistically significant (at the 90% confidence level), 26% reduction in the magnitude of GMST variability (Supplementary Fig. 11) between their pre-industrial control runs and the 2200–2300 time period of their RCP8.5 runs. This amounts to a ∼3% reduction in GMST variability per kelvin of climatological GMST warming. Also, qualitatively consistent with the GFDL CM3 model, the reduction in GMST variability largely emerges from a reduction in the high-latitude contribution to this variability (Supplementary Fig. 12a), which stems from a reduction in the ↓clear SW contribution to GMST variability (Supplementary Fig. 12c). It has been shown that CMIP5 model spread in the magnitude of GMST variability primarily originates from differences in simulated variability at high latitudes[45]. Thus, a proportionately larger reduction in high-latitude variability in a warmer climate also reduces inter-model spread in GMST variability (Supplementary Fig. 11).

The CMIP5 models investigated here, however, show a large diversity in their GMST variability response to climatological GMST warming. At one end of the range, MPI-ESM-LR, bcc-cms1-1 and CCSM4 simulate ∼55%, ∼50% and ∼44% reductions in GMST variability between their pre-industrial control and RCP8.5 runs (all ∼6% reduction per kelvin of climatological GMST warming). On the other end of the continuum, the CNRM-CM5 model shows a ∼7% increase in GMST variability between the two runs (∼1% increase per kelvin of GMST warming). Future work is required to understand this range of model behaviour.

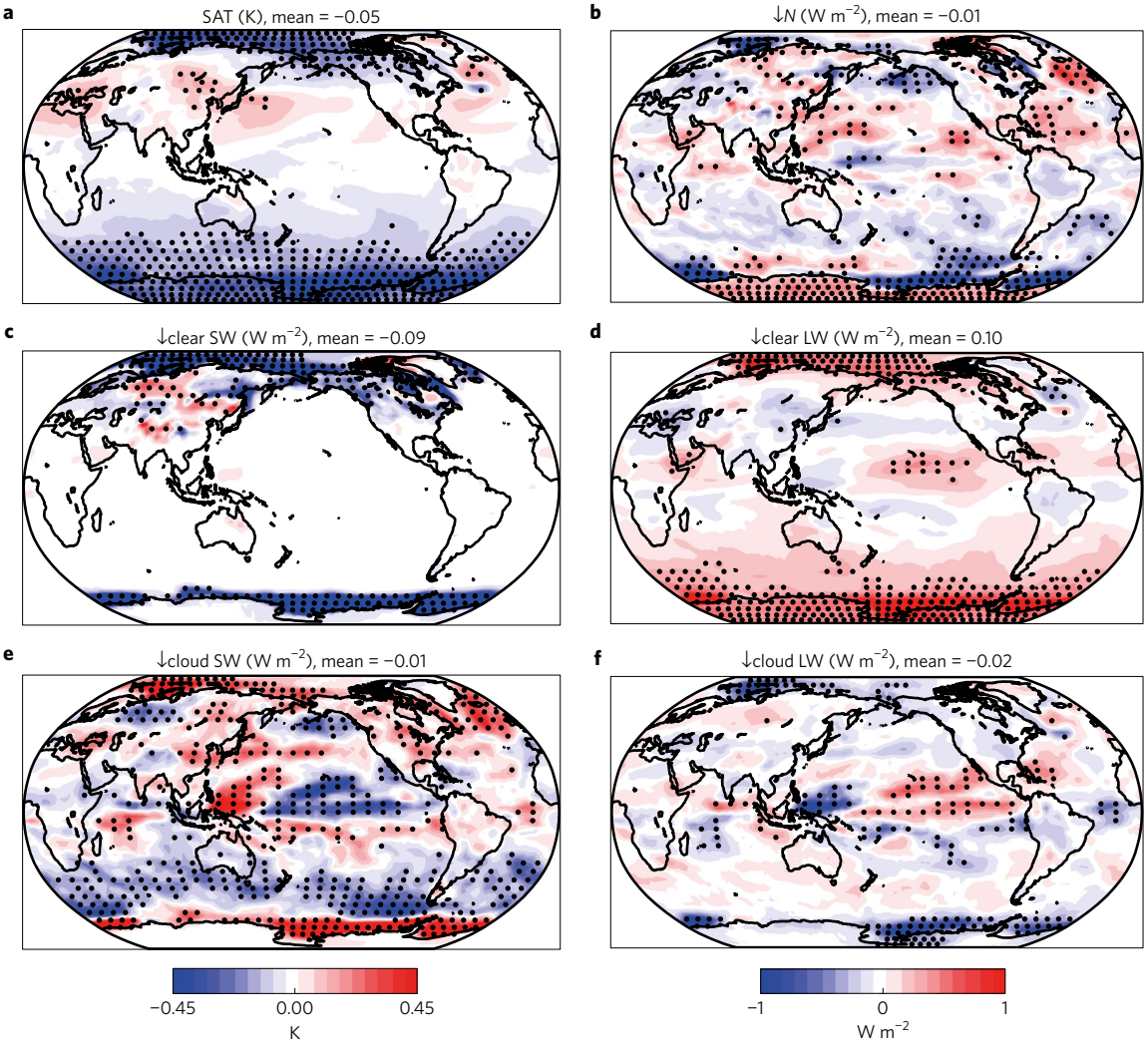

Figure 3 | Change in the TOA energy budget contribution to GMST variability between the GFDL CM3 pre-industrial control and 2 × CO_2 runs. **a**–**f**, Change in the local regression against the standard deviation of GMST for surface air temperature (**a**), net top-of-atmosphere radiative imbalance (**b**), clear-sky short-wave top-of-atmosphere radiative imbalance (**c**), clear-sky long-wave top-of-atmosphere radiative imbalance (**d**), short-wave cloud radiative effect (**e**) and long-wave cloud radiative effect (**f**). The global mean value of the variable is displayed for each panel. Stippling in panels represents statistically significant differences in regression coefficients calculated using a Monte Carlo technique (see Methods).

Changes in local surface temperature variability

Previous studies have indicated that SAT variability may increase over certain locations with warming[26–32]. Therefore, it is of interest to investigate whether the noted decrease in GMST variability apparent in GFDL CM3 and the CMIP5 experiments applies uniformly to the entirety of the Earth's surface or if there is substantial spatial heterogeneity. Figure 4a shows the fractional change in local low-frequency SAT variability between the pre-industrial control and 2 × CO_2 runs of GFDL CM3. Consistent with the results above, there is a large decrease in local variability over the Arctic and Southern oceans associated with a reduction in climatological sea-ice extent. The reduction of sea ice should reduce local SAT variability both because it reduces the propensity for albedo variability but also because the open ocean represents greatly enhanced surface heat capacity compared with sea ice[32].

In contrast to the reduced SAT variability at high latitudes, a large fraction of tropical and subtropical land areas actually experience an increase in variability between the pre-industrial control and 2 × CO_2 runs. A similar effect is also seen in a supplementary model run where a free-running atmosphere was forced with a uniform +4 K increase in sea surface temperatures (SSTs; Fig. 4c, see Methods) as well as in the CMIP5 ensemble mean (Supplementary Fig. 13a). The consistency of this effect between these different sets of experiments indicates that the enhancement of local SAT variability over some land regions is primarily driven by the climatological warming itself rather than resulting from particular changes in large-scale ocean–atmosphere–sea-ice modes of variability or in the spatial pattern of sea surface temperature warming.

To illuminate the first-order causes of locally increased land SAT variability, we compare mean changes in the surface energy budget between land locations in which low-frequency SAT variability increases with warming and land locations in which low-frequency SAT variability decreases with warming in the two GFDL model experiments (Fig. 4b,d) and in the CMIP5 runs (Supplementary Fig. 13b). In all experiments, there is little difference in climatological radiative surface energy availability ($\downarrow R_s$, see Methods) between the locations where SAT variability increases and the locations where SAT variability decreases (that is, $\downarrow R_s$ changes similarly in Fig. 4b, $\downarrow R_s$ changes similarly in Fig. 4d and $\downarrow R_s$ changes similarly in Supplementary Fig. 13b). However, in all experiments, climatological sensible heating (↑SH) increases more and climatological latent heating (↑LE) increases less over locations where SAT variability increases (Fig. 4c,d and Supplementary Fig. 14b). This can be partially explained by moisture availability

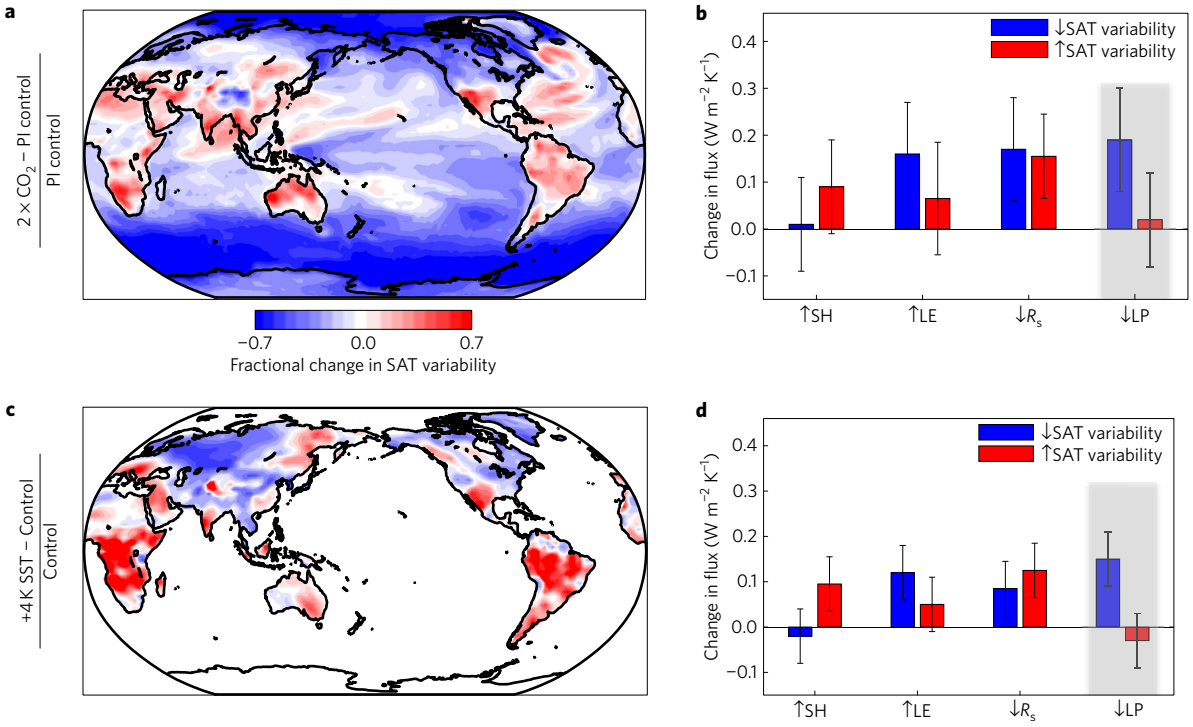

Figure 4 | Change in local temperature variability. a, Fractional change in the local temporal standard deviation of low-frequency SAT between the GFDL CM3 pre-industrial control and 2 × CO_2 runs (unitless). **b**, Change in the climatological energy flux (W m^{-2} K^{-1}) over land regions that experienced an increase in SAT variability (red) and land regions that experienced a decrease in SAT variability (blue) between the GFDL CM3 pre-industrial control and 2 × CO_2 runs. **c**, As in **a** but the fractional change between the GFDL AM3 observed SST run and +4 K SST run (see Methods). **d**, As in **b** but change between the GFDL AM3 observed SST run and +4 K SST run. In **b** and **d** ↑SH is upward sensible heat flux, ↑LE is upward latent heat flux, ↓R_s is the net downward radiation, and ↓LP is the latent heat of vaporization times the precipitation. ↓LP is shaded grey to indicate that it is not formally part of the energy budget but is used here as a proxy for water availability. The vertical error bars represent the standard error across all grid points accounting for spatial autocorrelation (see Methods).

(approximated here as precipitation multiplied by the latent heat of vaporization, ↓LP), which increases less over regions where SAT variability increases. Thus, land regions where local SAT variability increases tend to be regions where moisture availability declines with warming. Over these locations, incident radiation variability is able to have a stronger influence on SAT variability, because proportionally more incident radiation is converted to sensible (rather than latent) heat flux[46]. Many low- to mid-latitude land regions should fit this description, since land amplification of warming is likely to cause an increase in aridity[24,46–48].

Discussion

We show here that the magnitude of low-frequency unforced GMST variability is substantially reduced in the GFDL CM3 climate model after a doubling of CO_2 from pre-industrial levels and that the mechanisms responsible for that variability are fundamentally altered. In particular, the modes of variability primarily responsible for generating GMST variability are shifted in space, and the net flow of energy associated with unforced warming events changes from being into the climate system to out of the climate system (vice versa for unforced cooling events). We find that a primary reason for this shift is the reduction in high-latitude surface albedo variability that results from a climatological reduction in albedo. Finally, we find that local variability over many tropical and subtropical land areas increases with global warming despite the reduction in GMST variability.

A number of caveats should be stressed with regard to this study. Reasons for caution include the attribute that the GFDL CM3 model has unusually large GMST variability in its pre-industrial control run[5] as well as a 2 × CO_2 climate sensitivity towards the upper range of the CMIP5 ensemble range[49]. Taken together, these features may indicate that the reduction of GMST variability with a doubling of CO_2 may be exaggerated in GFDL CM3 compared with reality. As discussed above, the CMIP5 models investigated here show a smaller mean change in unforced GMST variability between their pre-industrial control and RCP8.5 runs (~3% per kelvin of climatological GMST warming on average compared with ~9% per kelvin of climatological GMST warming in GFDL CM3). Also, climate models differ substantially in the geographic origin and generating mechanisms of their unforced GMST variability[5], and thus changes in the generating mechanisms of GMST variability are likely to vary substantially from model to model.

Thus, we emphasize that the results from the GFDL CM3 model should not necessarily be interpreted as a robust quantitative forecast of future variability change. Instead the results of this study serve to demonstrate that the magnitude and mechanisms of unforced GMST variability may depend critically on the climatological GMST. This finding indicates that some traditional means of studying GMST variability (for example, investigating pre-industrial control runs or palaeo-reconstructions of past variability) may be of limited utility for surmising information on the behaviour of unforced GMST variability in a warmer climate.

Methods

Methods, including statements of data availability and any associated accession codes and references, are available in the online version of this paper.

Received 13 October 2016; accepted 3 August 2017; published online 4 September 2017

References

1. Bindoff, N. L. *et al*. In *Climate Change 2013: The Physical Science Basis* (eds Stocker, T. F. *et al*.) Ch. 10 (IPCC, Cambridge Univ. Press, 2013).
2. Hawkins, E. & Sutton, R. The potential to narrow uncertainty in regional climate predictions. *Bull. Am. Meteorol. Soc.* **90,** 1095–1107 (2009).
3. Meehl, G. A. *et al*. Decadal prediction. *Bull. Am. Meteorol. Soc.* **90,** 1467–1485 (2009).
4. Hasselmann, K. Stochastic climate models. Part I. Theory. *Tellus* **28,** 473–485 (1976).
5. Brown, P. T., Li, W. & Xie, S.-P. Regions of significant influence on unforced global mean surface air temperature variability in climate models. *J. Geophys. Res.* **120,** 480–494 (2015).
6. Brown, P. T., Li, W., Li, L. & Ming, Y. Top-of-atmosphere radiative contribution to unforced decadal global temperature variability in climate models. *Geophys. Res. Lett.* **41,** 5175–5183 (2014).
7. Knutson, T. R., Zhang, R. & Horowitz, L. W. Prospects for a prolonged slowdown in global warming in the early 21st century. *Nat. Commun.* **7,** 13676 (2016).
8. Huber, M. & Knutti, R. Natural variability, radiative forcing and climate response in the recent hiatus reconciled. *Nat. Geosci.* **7,** 651–656 (2014).
9. Roberts, C. D., Palmer, M. D., McNeall, D. & Collins, M. Quantifying the likelihood of a continued hiatus in global warming. *Nat. Clim. Change* **5,** 337–342 (2015).
10. Middlemas, E. & Clement, A. M. Y. Spatial patterns and frequency of unforced decadal-scale changes in global mean surface temperature in climate models. *J. Clim.* **29,** 6245–6257 (2016).
11. Brown, P. T., Li, W., Cordero, E. C. & Mauget, S. A. Comparing the model-simulated global warming signal to observations using empirical estimates of unforced noise. *Sci. Rep.* **5,** 9957 (2015).
12. Schurer, A. P., Hegerl, G. C., Mann, M. E., Tett, S. F. B. & Phipps, S. J. Separating forced from chaotic climate variability over the past millennium. *J. Clim.* **26,** 6954–6973 (2013).
13. Crowley, T. J., Obrochta, S. P. & Liu, J. Recent global temperature 'plateau' in the context of a new proxy reconstruction. *Earth's Future* **2,** 281–294 (2014).
14. Jones, G. S., Stott, P. A. & Christidis, N. Attribution of observed historical near-surface temperature variations to anthropogenic and natural causes using CMIP5 simulations. *J. Geophys. Res.* **118,** 4001–4024 (2013).
15. Crowley, T. J. Causes of climate change over the past 1,000 years. *Science* **289,** 270–277 (2000).
16. Mann, M. E., Steinman, B. A. & Miller, S. K. On forced temperature changes, internal variability and the AMO. *Geophys. Res. Lett.* **41,** 3211–3219 (2014).
17. Muller, R. A. *et al*. Decadal variations in the global atmospheric land temperatures. *J. Geophys. Res.* **118,** 5280–5286 (2013).
18. Meehl, G. A., Teng, H. & Arblaster, J. M. Climate model simulations of the observed early-2000s hiatus of global warming. *Nat. Clim. Change* **4,** 898–902 (2014).
19. Santer, B. D. *et al*. Separating signal and noise in atmospheric temperature changes: the importance of timescale. *J. Geophys. Res.* **116,** D22105 (2011).
20. Risbey, J. S. Well-estimated global surface warming in climate projections selected for ENSO phase. *Nat. Clim. Change* **4,** 835–840 (2014).
21. Maher, N., Gupta, A. S. & England, M. H. Drivers of decadal hiatus periods in the 20th and 21st centuries. *Geophys. Res. Lett.* **41,** 5978–5986 (2014).
22. Collins, M. *et al*. In *Climate Change 2013: The Physical Science Basis* (eds Stocker, T. F. *et al*.) Ch. 12 (IPCC, Cambridge Univ. Press, 2013).
23. de Lavergne, C., Palter, J. B., Galbraith, E. D., Bernardello, R. & Marinov, I. Cessation of deep convection in the open Southern Ocean under anthropogenic climate change. *Nat. Clim. Change* **4,** 278–282 (2014).
24. Joshi, M. M., Gregory, J. M., Webb, M. J., Sexton, D. M. H. & Johns, T. C. Mechanisms for the land/sea warming contrast exhibited by simulations of climate change. *Clim. Dynam.* **30,** 455–465 (2007).
25. Huntingford, C., Jones, P. D., Livina, V. N., Lenton, T. M. & Cox, P. M. No increase in global temperature variability despite changing regional patterns. *Nature* **500,** 327–330 (2013).
26. Räisänen, J. CO_2-induced changes in interannual temperature and precipitation variability in 19 CMIP2 experiments. *J. Clim.* **15,** 2395–2411 (2002).
27. Boer, J. G., Flato, G. & Ramsden, D. A transient climate change simulation with greenhouse gas and aerosol forcing: projected climate to the twenty-first century. *Clim. Dynam.* **16,** 427–450 (2000).
28. Meehl, G. A., Wheeler, M. & Washington, W. M. Low-frequency variability and CO_2 transient climate change. Part 3. Intermonthly and interannual variability. *Clim. Dynam.* **10,** 277–303 (1994).
29. Rind, D., Goldberg, R. & Ruedy, R. Change in climate variability in the 21st century. *Climatic Change* **14,** 5–37 (1989).
30. Sakai, D., Itoh, H. & Yukimoto, S. Changes in the interannual surface air temperature variability in the Northern Hemisphere in response to global warming. *J. Meteorol. Soc. Jpn* **87,** 721–737 (2009).
31. Boer, G. J. Changes in interannual variability and decadal potential predictability under global warming. *J. Clim.* **22,** 3098–3109 (2009).
32. Stouffer, R. J. & Wetherald, R. T. Changes of variability in response to increasing greenhouse gases. Part I: temperature. *J. Clim.* **20,** 5455–5467 (2007).
33. Taylor, K. E., Stouffer, R. J. & Meehl, G. A. An overview of CMIP5 and the experiment design. *Bull. Am. Meteorol. Soc.* **93,** 485–498 (2011).
34. Cleveland, W. S. Robust locally weighted regression and smoothing scatterplots. *J. Am. Stat. Assoc.* **74,** 829–836 (1979).
35. England, M. H. *et al*. Recent intensification of wind-driven circulation in the Pacific and the ongoing warming hiatus. *Nat. Clim. Change* **4,** 222–227 (2014).
36. Chen, X. & Tung, K.-K. Varying planetary heat sink led to global-warming slowdown and acceleration. *Science* **345,** 897–903 (2014).
37. Drijfhout, S. S. *et al*. Surface warming hiatus caused by increased heat uptake across multiple ocean basins. *Geophys. Res. Lett.* **41,** 7868–7874 (2014).
38. Meehl, G. A., Hu, A., Arblaster, J. M., Fasullo, J. & Trenberth, K. E. Externally forced and internally generated decadal climate variability associated with the interdecadal Pacific oscillation. *J. Clim.* **26,** 7298–7310 (2013).
39. Xie, S.-P., Kosaka, Y. & Okumura, Y. M. Distinct energy budgets for anthropogenic and natural changes during global warming hiatus. *Nat. Geosci.* **9,** 29–33 (2016).
40. Hedemann, C., Mauritsen, T., Jungclaus, J. & Marotzke, J. The subtle origins of surface-warming hiatuses. *Nat. Clim. Change* **7,** 336–339 (2017).
41. Pedro, J. B. *et al*. Southern Ocean deep convection as a driver of Antarctic warming events. *Geophys. Res. Lett.* **43,** 2192–2199 (2016).
42. Behrens, E. *et al*. Southern Ocean deep convection in global climate models: a driver for variability of subpolar gyres and Drake Passage transport on decadal timescales. *J. Geophys. Res.* **121,** 3905–3925 (2016).
43. Martin, T., Park, W. & Latif, M. Multi-centennial variability controlled by Southern Ocean convection in the Kiel Climate Model. *Clim. Dynam.* **40,** 2005–2022 (2013).
44. Brown, P. T., Lozier, M. S., Zhang, R. & Li, W. The necessity of cloud feedback for a basin-scale Atlantic Multidecadal Oscillation. *Geophys. Res. Lett.* **43,** 3955–3963 (2016).
45. Brown, P. T., Li, W., Jiang, J. H. & Su, H. Spread in the magnitude of climate model interdecadal global temperature variability traced to disagreements over high-latitude oceans. *Geophys. Res. Lett.* **43,** 12543–12549 (2016).
46. Sherwood, S. & Fu, Q. A drier future? *Science* **343,** 737–739 (2014).
47. Byrne, M. P. & O'Gorman, P. A. Link between land-ocean warming contrast and surface relative humidities in simulations with coupled climate models. *Geophys. Res. Lett.* **40,** 5223–5227 (2013).
48. Berg, A. *et al*. Land–atmosphere feedbacks amplify aridity increase over land under global warming. *Nat. Clim. Change* **6,** 869–874 (2016).
49. Flato, G. J. *et al*. In *Climate Change 2013: The Physical Science Basis* (eds Stocker, T. F. *et al*.) Ch. 9 (IPCC, Cambridge Univ. Press, 2013).

Acknowledgements

We would like to acknowledge M. Winton and T. Knutson for internal reviews and discussion of this work. We acknowledge the World Climate Research Programme's Working Group on Coupled Modelling, which is responsible for CMIP, and we thank the climate modelling groups for producing and making available their model output. For CMIP, the US Department of Energy's Program for Climate Model Diagnosis and Intercomparison provides coordinating support and led development of software infrastructure in partnership with the Global Organization for Earth System Science Portals. This research was partially conducted at the NOAA Geophysical Fluid Dynamics Laboratory, Princeton, New Jersey and it was partially supported by NIH-1R21AG044294-01A1. S.A.H. was supported by a Department of Defense National Defense Science and Engineering Graduate Fellowship and a National Science Foundation Atmospheric and Geospace Sciences Postdoctoral Research Fellowship.

Author contributions

Y.M. conceived of the study. S.A.H. proposed and conducted the fixed SST model runs. P.T.B. performed the data analysis and wrote the initial draft of the manuscript. All authors contributed to interpreting results and refinement of the manuscript.

Additional information

Supplementary information is available in the online version of the paper. Reprints and permissions information is available online at www.nature.com/reprints. Publisher's note: Springer Nature remains neutral with regard to jurisdictional claims in published maps and institutional affiliations. Correspondence and requests for materials should be addressed to P.T.B.

Competing financial interests

The authors declare no competing financial interests.

Methods

Removal of model drift. All GFDL model data were detrended at the grid level with empirical mode decomposition[50,51], preventing non-physical model drift from contaminating our analysis of variability.

Low-frequency variability. We define the low-frequency component of variability using a 15-year lowess smooth[34] of a given time series. The conclusions of this study are unaltered when using a different filter (15-year running mean) and/or a different timescale (25 years).

Pre-industrial versus 2 × CO_2 runs of the coupled GFDL CM3 model. GFDL CM3 is a coupled climate model with dynamic ocean, atmosphere, sea-ice[52] and land[53,54] components[55–57]. The ocean model has a 1° tripolar 360 × 200 horizontal resolution, with 50 levels in the vertical[52]. The atmospheric model utilizes a 200 km horizontal resolution (C48L48) with 48 vertical levels up to 0.01 hPa (ref. 56). The coupled model features interactive aerosol[58] and atmospheric chemistry[59] but does not simulate ocean biogeochemistry or ice-sheet dynamics. We investigate changes in unforced variability between GFDL CM3's pre-industrial control run and a run that has experienced a doubling of CO_2 from pre-industrial values (1% yr^{-1}) and has reached a new equilibrium state. We use the last 860 years of each run to ensure that the models were near equilibration. This meant that we omitted the first 220 years from the 1,080-year pre-industrial control run and the first 1,920 years from the 2,780 year 1% yr^{-1} 2 × CO_2 run, the latter so as not to include the transient warming phase and the subsequent slow equilibration to the new boundary conditions.

AMO. We define the AMO as the low-frequency component of the spatially weighted mean sea surface temperature between 7.5° W and 75° W and 0° and 65° N in the Atlantic Ocean.

Current SST versus uniform +4 K SST of the GFDL AM3 model. To isolate the role of atmospheric/surface process from the role ocean–atmosphere–sea-ice processes, we conduct an experiment set where the atmospheric component of GFDL CM3 (AM3) is forced by annually repeating climatological seasonal cycles of SSTs and sea ice (Fig. 4c,d). We compare a run forced with a climatological seasonal cycle of SSTs and sea ice[60] repeated annually to an identical run but with a uniform +4 K increase of SSTs. In the +4 K SST run, sea ice and vegetation were held constant. We investigate 200 years of variability in this experiment set. Note that GMST change in the uniform SST warming run (4.6 K) is very similar to the magnitude of the GMST change between the pre-industrial control and 2 × CO_2 coupled model runs (4.8 K).

Change in unforced variability with warming in CMIP5 runs. The CMIP5 experiment design did not include equilibrated runs under a 2 × CO_2 condition and thus it was impossible to directly compare results between the GFDL CM3 experiment and other CMIP5 models. However, as a substitution for a direct comparison, we investigate how unforced low-frequency variability changed in fully coupled CMIP5 models between their pre-industrial control runs (first 200 years) and the years 2200–2300 of their RCP8.5 runs. The post-2200 time period was selected because there is little change in radiative forcing thereafter[61]. However, models are not equilibrated in the year 2200. Thus, to isolate unforced variability from forced variability, we regress-out the multi-model mean of a given variable's response at the grid level. Both the pre-industrial control and RCP8.5 time periods were also subjected to detrending using empirical mode decomposition to ensure time series were stationary prior to further analysis[50,51]. Nine CMIP5 models were available (with our required variables) with both pre-industrial control and post-2200 RCP8.5 data archived (Supplementary Table 1).

Components of $\downarrow N$. The net anomalous top-of-atmosphere energy imbalance, $\downarrow N$ (W m^{-2}), can be decomposed into four linearly additive components ($\downarrow N = [\downarrow\text{clear SW}] + [\downarrow\text{clear LW}] + [\downarrow\text{cloud SW}] + [\downarrow\text{cloud LW}]$)[62], where

$$\downarrow\text{clear SW} = [\downarrow\text{SW} - \uparrow\text{SW}_{\text{clearsky}}] \quad (1)$$

$$\downarrow\text{clear LW} = [-\uparrow\text{LW}_{\text{clearsky}}] \quad (2)$$

$$\downarrow\text{cloud SW} = [\downarrow\text{SW} - \uparrow\text{SW}_{\text{allsky}}] - [\downarrow\text{SW} - \uparrow\text{SW}_{\text{clearsky}}]$$
$$= \uparrow\text{SW}_{\text{clearsky}} - \uparrow\text{SW}_{\text{allsky}} \quad (3)$$

$$\downarrow\text{cloud LW} = [-\uparrow\text{LW}_{\text{allsky}}] - [-\uparrow\text{LW}_{\text{clearsky}}]$$
$$= \uparrow\text{LW}_{\text{clearsky}} - \uparrow\text{LW}_{\text{allsky}} \quad (4)$$

Clear SW is the clear-sky short-wave component, clear LW is the clear-sky long-wave component, cloud SW is the short-wave cloud radiative effect and cloud LW is the long-wave cloud radiative effect.

Surface energy budget. The surface energy budget is defined in the typical way,

$$\uparrow Q = [\uparrow\text{LE}] + [\uparrow\text{LH}] + [\uparrow\text{SW} - \downarrow\text{SW}] + [\uparrow\text{LW} - \downarrow\text{LW}] \quad (5)$$

In Fig. 4, $\downarrow R_s$ is the downward-oriented net radiative imbalance,

$$\downarrow R_s = [\downarrow\text{SW} - \uparrow\text{SW}] + [\downarrow\text{LW} - \uparrow\text{LW}] \quad (6)$$

Confidence intervals for cross-regressions of Fig. 2. To create the confidence intervals for the cross-regression coefficients shown in Fig. 2, we used the Monte Carlo method described in the following steps: at each time lag, AR(2) noise models were fitted to both sub-samples of the time series under consideration using Akaike information criterion; 10,000 synthetic time series were created for each of the two input samples; all time series were smoothed using a 15-year lowess filter; 10,000 regression coefficients were calculated between the two groups of synthetic time series; the 5th/95th percentile range of the regression coefficients was used as the range of the confidence interval.

Statistical significance of changes in local regression coefficients against GMST in Fig. 3. To identify statistically significant changes in the regression coefficients against GMST between GFDL CM3's 2 × CO_2 and pre-industrial control runs (Fig. 3), we used the Monte Carlo method described in the following steps: AR(2) noise models were fitted to both sets of time series under consideration for both runs (four noise models in total) using the Akaike information criterion; 10,000 synthetic time series were created for each of the two input time series for each run (40,000 times series in total); time series were smoothed using a 15-year lowess filter; 10,000 regression coefficients were calculated between the two time series for each run (20,000 regression coefficients in total); a distribution of the difference between the regression coefficients was created; the 5th and 95th percentiles of the difference distribution were noted; if the measured difference in the regression coefficients was less than the 5th percentile or greater than the 95th percentile of the synthetic distribution, that difference was deemed to be statistically significant.

Error bars in Fig. 4b,d. Figure 4b,d displays standard errors of the mean differences between the model runs for a number of variables. These standard errors were calculated so that they accounted for spatial autocorrelation in the following way: for a given variable (for example, sensible heat flux), the map of the difference between the two runs was considered; at each latitude between 70° N and 70° S, the decorrelation length scale in the zonal direction was computed (the decorrelation length scale was defined as the number of grid points that it took for the spatial autocorrelation function to drop below $1/e$); the map-mean decorrelation length scale was calculated by averaging together the zonal decorrelation length scales with cosine weights; the effective number of independent grid points on the map (N_{eff}) was then calculated as the original number of grid points divided by the map-mean decorrelation length scale; N_{eff} was then used in the calculation of the standard error.

Data availability. The CMIP5 data used for this study can be downloaded at http://cmip-pcmdi.llnl.gov/cmip5/data_portal.html and the GFDL model data can be downloaded at http://nomads.gfdl.noaa.gov:8080/DataPortal/cmip5.jsp. Other data that support the findings of this study are available from the corresponding author upon request.

References

50. Huang, N. E. *et al*. The empirical mode decomposition and the Hilbert spectrum for nonlinear and non-stationary time series analysis. *Proc. R. Soc. Lond. A* **454,** 903–995 (1998).
51. Wu, Z., Huang, N. E., Long, S. R. & Peng, C.-K. On the trend, detrending, and variability of nonlinear and nonstationary time series. *Proc. Natl Acad. Sci. USA* **104,** 14889–14894 (2007).
52. Griffies, S. M. & Greatbatch, R. J. Physical processes that impact the evolution of global mean sea level in ocean climate models. *Ocean Model.* **51,** 37–72 (2012).
53. Milly, P. C. D. & Shmakin, A. B. Global modeling of land water and energy balances. Part I: the land dynamics (LaD) model. *J. Hydrometeorol.* **3,** 283–299 (2002).
54. Shevliakova, E. *et al*. Carbon cycling under 300 years of land use change: importance of the secondary vegetation sink. *Glob. Biogeochem. Cycles* **23,** 3520–3544 (2009).

55. Griffies, S. M. *et al*. The GFDL CM3 coupled climate model: characteristics of the ocean and sea ice simulations. *J. Clim.* **24,** 3520–3544 (2011).
56. Donner, L. J. *et al*. The dynamical core, physical parameterizations, and basic simulation characteristics of the atmospheric component AM3 of the GFDL global coupled model CM3. *J. Clim.* **24,** 3484–3519 (2011).
57. Delworth, T. L. *et al*. GFDL's CM2 global coupled climate models. Part I: formulation and simulation characteristics. *J. Clim.* **19,** 643–674 (2006).
58. Levy, H. *et al*. The roles of aerosol direct and indirect effects in past and future climate change. *J. Geophys. Res.* **118,** 4521–4532 (2013).
59. Austin, J. & Wilson, R. J. Ensemble simulations of the decline and recovery of stratospheric ozone. *J. Geophys. Res.* **111,** 5145–5153 (2006).
60. Hurrell, J. W., Hack, J. J., Shea, D., Caron, J. M. & Rosinski, J. A new sea surface temperature and sea ice boundary dataset for the community atmosphere model. *J. Clim.* **21,** 5145–5153 (2008).
61. Meinshausen, M. *et al*. The RCP greenhouse gas concentrations and their extensions from 1765 to 2300. *Climatic Change* **109,** 213–241 (2011).
62. Ramanathan, V. *et al*. Cloud-radiative forcing and climate: results from the Earth radiation budget experiment. *Science* **243,** 57–63 (1989).